

# Precision Measurement of the Specific Activity of $^{39}\text{Ar}$ in Atmospheric Argon with the DEAP-3600 Detector

P. Adhikari<sup>6</sup>, R. Ajaj<sup>6,28</sup>, M. Alpízar-Venegas<sup>15</sup>, P.-A. Amaudruz<sup>26</sup>, J. Anstey<sup>6,28</sup>, G.R. Araujo<sup>27</sup>, D.J. Auty<sup>1</sup>, M. Baldwin<sup>23</sup>, M. Batygov<sup>13</sup>, B. Beltran<sup>1</sup>, H. Benmansour<sup>21</sup>, C.E. Bina<sup>1,28</sup>, J. Bonatt<sup>21</sup>, W. Bonivento<sup>10</sup>, M.G. Boulay<sup>6</sup>, B. Broerman<sup>21</sup>, J.F. Bueno<sup>1</sup>, P.M. Burghardt<sup>27</sup>, A. Butcher<sup>22</sup>, M. Cadeddu<sup>10</sup>, B. Cai<sup>6,28</sup>, M. Cárdenas-Montes<sup>7</sup>, S. Cavioti<sup>9,28</sup>, M. Chen<sup>21</sup>, Y. Chen<sup>1</sup>, S. Choudhary<sup>2</sup>, B.T. Cleveland<sup>24,13</sup>, J.M. Corning<sup>21</sup>, R. Crampton<sup>6,28</sup>, D. Cranshaw<sup>21</sup>, S. Daugherty<sup>24,13</sup>, P. DelGobbo<sup>6,28</sup>, K. Dering<sup>21</sup>, P. Di Stefano<sup>21</sup>, J. DiGiuseffo<sup>6</sup>, G. Dolganov<sup>17,18</sup>, L. Doria<sup>20</sup>, F.A. Duncan<sup>24,a</sup>, M. Dunford<sup>6,28</sup>, E. Ellingwood<sup>21</sup>, A. Erlandson<sup>6,4</sup>, S.S. Farahani<sup>1</sup>, N. Fatemighomi<sup>24,22</sup>, G. Fiorillo<sup>8,12</sup>, S. Florian<sup>21</sup>, A. Flower<sup>6,21</sup>, R.J. Ford<sup>24,13</sup>, R. Gagnon<sup>21</sup>, D. Gallacher<sup>6</sup>, P. García Abia<sup>7</sup>, S. Garg<sup>6</sup>, P. Giampa<sup>21,26</sup>, A. Giménez-Alcázar<sup>7</sup>, D. Goeldi<sup>6,28</sup>, V.V. Golovko<sup>4,21</sup>, P. Gorel<sup>24,13</sup>, K. Graham<sup>6</sup>, D.R. Grant<sup>1</sup>, A. Grobov<sup>17</sup>, A.L. Hallin<sup>1</sup>, M. Hamstra<sup>6,21</sup>, P.J. Harvey<sup>21</sup>, S. Haskins<sup>6,28</sup>, C. Hearn<sup>21</sup>, J. Hu<sup>1</sup>, J. Hucker<sup>21</sup>, T. Hugues<sup>2</sup>, A. Ilyasov<sup>17,18</sup>, B. Jigmeddorj<sup>13,4</sup>, C.J. Jillings<sup>24,13</sup>, A. Joy<sup>1,28</sup>, O. Kamaev<sup>4</sup>, G. Kaur<sup>6</sup>, A. Kemp<sup>22,21</sup>, M. Kuźniak<sup>2,6,28</sup>, F. La Zia<sup>22</sup>, M. Lai<sup>3,10</sup>, S. Langrock<sup>13,28</sup>, B. Lehnert<sup>14</sup>, A. Leonhardt<sup>27</sup>, J. LePage-Bourbonnais<sup>6,28</sup>, N. Levashko<sup>17</sup>, J. Lidgard<sup>21</sup>, T. Lindner<sup>26</sup>, M. Lissia<sup>10</sup>, J. Lock<sup>6</sup>, I. Machulin<sup>17,18</sup>, P. Majewski<sup>23</sup>, A. Maru<sup>6,28</sup>, J. Mason<sup>6,28</sup>, A.B. McDonald<sup>21</sup>, T. McElroy<sup>1</sup>, T. McGinn<sup>6,21,a</sup>, J.B. McLaughlin<sup>22,26</sup>, R. Mehdiyev<sup>6</sup>, C. Mielnichuk<sup>1,10</sup>, L. Mirasola<sup>3,10</sup>, J. Monroe<sup>22</sup>, P. Nadeau<sup>6</sup>, C. Nantais<sup>21</sup>, C. Ng<sup>1</sup>, A.J. Noble<sup>21</sup>, E. O'Dwyer<sup>21</sup>, G. Oliviero<sup>6,28</sup>, C. Ouellet<sup>6</sup>, S. Pal<sup>1,28</sup>, D. Papi<sup>1</sup>, P. Pasuthip<sup>21</sup>, S.J.M. Peeters<sup>25</sup>, M. Perry<sup>6</sup>, V. Pesudo<sup>7</sup>, E. Picciau<sup>10,3</sup>, M.-C. Piro<sup>1,28</sup>, T.R. Pollmann<sup>27,13</sup>, F. Rad<sup>6,28</sup>, E.T. Rand<sup>4</sup>, C. Rethmeier<sup>6</sup>, F. Retière<sup>26</sup>, I. Rodríguez García<sup>7</sup>, L. Roszkowski<sup>2,16</sup>, J.B. Ruhland<sup>27</sup>, R. Santorelli<sup>7</sup>, F.G. Schuckman II<sup>21</sup>, N. Seeburn<sup>22</sup>, S. Seth<sup>6,28</sup>, V. Shalamova<sup>5</sup>, K. Singhrao<sup>1</sup>, P. Skensved<sup>1</sup>, N.J.T. Smith<sup>24,13</sup>, B. Smith<sup>26</sup>, K. Sobotkiewicz<sup>6</sup>, T. Sonley<sup>24,6</sup>, J. Sosiak<sup>6,28</sup>, J. Soukup<sup>1</sup>, R. Stainforth<sup>6</sup>, C. Stone<sup>21</sup>, V. Strickland<sup>26,6</sup>, M. Stringer<sup>21,28</sup>, B. Sur<sup>4</sup>, J. Tang<sup>1</sup>, E. Vázquez-Jáuregui<sup>15</sup>, L. Veloce<sup>21</sup>, S. Viel<sup>6,28</sup>, B. Vyas<sup>6</sup>, M. Walczak<sup>2</sup>, J. Walding<sup>22</sup>, M. Ward<sup>21</sup>, S. Westerdale<sup>5</sup>, J. Willis<sup>1</sup>, A. Zuñiga-Reyes<sup>15</sup> (DEAP Collaboration)<sup>b</sup>

<sup>1</sup> Department of Physics, University of Alberta, Edmonton, Alberta, T6G 2R3, Canada

<sup>2</sup> AstroCeNT, Nicolaus Copernicus Astronomical Center, Polish Academy of Sciences, Rektorska 4, 00-614 Warsaw, Poland

<sup>3</sup> Physics Department, Università degli Studi di Cagliari, Cagliari 09042, Italy

<sup>4</sup> Canadian Nuclear Laboratories, Chalk River, Ontario, K0J 1J0, Canada

<sup>5</sup> Department of Physics and Astronomy, University of California, Riverside, CA 92507, USA

<sup>6</sup> Department of Physics, Carleton University, Ottawa, Ontario, K1S 5B6, Canada

<sup>7</sup> Centro de Investigaciones Energéticas, Medioambientales y Tecnológicas, Madrid 28040, Spain

<sup>8</sup> Physics Department, Università degli Studi "Federico II" di Napoli, Napoli 80126, Italy

<sup>9</sup> Astronomical Observatory of Capodimonte, Salita Moiariello 16, I-80131 Napoli, Italy

<sup>10</sup> INFN Cagliari, Cagliari 09042, Italy

<sup>11</sup> INFN Laboratori Nazionali del Gran Sasso, Assergi (AQ) 67100, Italy

<sup>12</sup> INFN Napoli, Napoli 80126, Italy

<sup>13</sup> School of Natural Sciences, Laurentian University, Sudbury, Ontario, P3E 2C6, Canada

<sup>14</sup> Nuclear Science Division, Lawrence Berkeley National Laboratory, Berkeley, CA 94720, USA

<sup>15</sup> Instituto de Física, Universidad Nacional Autónoma de México, A. P. 20-364, Ciudad de México 01000, Mexico

<sup>16</sup> BP2, National Centre for Nuclear Research, ul. Pasteura 7, 02-093 Warsaw, Poland

<sup>17</sup> National Research Centre Kurchatov Institute, Moscow 123182, Russia

<sup>18</sup> National Research Nuclear University MEPhI, Moscow 115409, Russia

<sup>19</sup> Physics Department, Princeton University, Princeton, NJ 08544, USA

<sup>20</sup> PRISMA<sup>+</sup> Cluster of Excellence and Institut für Kernphysik, Johannes Gutenberg-Universität Mainz, 55128 Mainz, Germany

<sup>21</sup> Department of Physics, Engineering Physics and Astronomy, Queen's University, Kingston, Ontario, K7L 3N6, Canada

<sup>22</sup> Royal Holloway University London, Egham Hill, Egham, Surrey, TW20 0EX, United Kingdom

<sup>23</sup> Rutherford Appleton Laboratory, Harwell Oxford, Didcot OX11 0QX, United Kingdom

<sup>24</sup> SNOLAB, Lively, Ontario, P3Y 1M3, Canada

<sup>25</sup> University of Sussex, Sussex House, Brighton, East Sussex, BN1 9RH, United Kingdom

<sup>26</sup> TRIUMF, Vancouver, British Columbia, V6T 2A3, Canada

<sup>27</sup> Department of Physics, Technische Universität München, 80333 Munich, Germany

<sup>28</sup> Arthur B. McDonald Canadian Astroparticle Physics Research Institute, Queen's University, Kingston, ON, K7L 3N6, Canada

**Abstract** The specific activity of the beta decay of  $^{39}\text{Ar}$  in atmospheric argon is measured using the DEAP-3600 detector. DEAP-3600, located 2 km underground at SNOLAB, uses a total of  $(3269 \pm 24)$  kg of liquid argon distilled from the atmosphere to search for dark matter. This detector with very low background uses pulse shape discrimination to differentiate between nuclear recoils and electron recoils and is well-suited to measure the decay of  $^{39}\text{Ar}$ . With 167 live-days of data, the measured specific activity at the time of atmospheric extraction is  $[0.964 \pm 0.001 \text{ (stat)} \pm 0.024 \text{ (sys)}]$  Bq/kg<sub>atmAr</sub> which is consistent with results from other experiments. A cross-check analysis using different event selection criteria provides a consistent result.

**Keywords** Atmospheric argon · Beta decay · Specific activity ·  $^{39}\text{Ar}$  · DEAP-3600

## 1 Introduction

Argon is used as a target material in a variety of particle detectors [1–7]. Commercially available argon is obtained by distillation from the Earth’s atmosphere where it has a natural abundance of about 0.93% [8]. While atmospheric argon primarily consists of the stable isotope  $^{40}\text{Ar}$ , a small amount of cosmogenically created, radioactive  $^{39}\text{Ar}$  is also present and represents a background in low-threshold detectors. The isotope  $^{39}\text{Ar}$  decays via unique first-forbidden beta decay with a half-life of  $T_{1/2} = (269 \pm 3)$  years and a Q-value of  $(565 \pm 5)$  keV [9–11].

While the production of  $^{39}\text{Ar}$  in the atmosphere is in equilibrium, measurements of ice cores and tree rings by Gu et al. [12] show the  $^{39}\text{Ar}/\text{Ar}$  ratio has varied by as much as 17% in the past 2500 years. Recent measurements of the specific activity of  $^{39}\text{Ar}$  in atmospheric argon,  $S_{\text{Ar}39}$ , were realized by the WARP collaboration with a result of  $S_{\text{Ar}39} = (1.01 \pm 0.08)$  Bq/kg<sub>atmAr</sub> [13] and by the ArDM collaboration with  $S_{\text{Ar}39} = (0.95 \pm 0.05)$  Bq/kg<sub>atmAr</sub> [14].

This paper describes the measurement of the  $^{39}\text{Ar}$  specific activity using the DEAP-3600 detector [7], located 2 km underground in Creighton Mine at SNOLAB in Sudbury, Ontario, Canada. DEAP-3600 is a low-background dark matter experiment with a liquid argon (LAr) target and is described briefly in Section 2. The large mass of atmospheric argon and the very low background levels achieved with this experiment [15, 16] enable the precision specific activity measurement presented here. The specific activity is calculated by estimating the total number  $N$  of  $^{39}\text{Ar}$  decays within a certain live-time  $T_{\text{live}}$ :

$$S_{\text{Ar}39} = \frac{N}{T_{\text{live}} \cdot m_{\text{LAr}}}, \quad (1)$$

<sup>a</sup>Deceased.

<sup>b</sup>deap-papers@snolab.ca

where  $m_{\text{LAr}}$  is the mass of LAr in the detector.

A dedicated estimate of the LAr mass in DEAP-3600 is presented in Section 3. The dataset and livetime calculation, as well as the event selection are described in Section 4. The measurement of  $N$  is presented in Section 5, alongside details on the  $S_{\text{Ar}39}$  calculation, systematic uncertainties and results. Section 6 briefly describes an updated version of the measurement from Ref. [17] which appears here as a cross-check. Concluding remarks are given in Section 7.

## 2 The Detector and Data Acquisition System

The DEAP-3600 experiment operated with an ultra-pure LAr target of over 3 tonnes held in an 85 cm radius spherical acrylic vessel (AV) from November 2016 to April 2020. A detailed description of the DEAP-3600 detector is given in Ref. [7]. The atmospheric argon for the LAr target was procured from Air Liquide.

Connected to the top of the AV is an acrylic neck surrounding a liquid nitrogen ( $\text{LN}_2$ ) filled stainless steel cooling coil which condenses the gaseous argon (GAr) contained in the top of the AV. The AV was partially filled with the GAr/LAr interface approximately 55 cm above the equator. After filling with LAr the detector was sealed and this volume of argon remained within the AV for the duration of data taking. Cooling of the LAr was achieved by continuous circulation of  $\text{LN}_2$  within the cooling coil.

Coated on the inner surface of the AV is a layer of tetraphenyl butadiene (TPB) which wavelength-shifts the ultraviolet (UV) scintillation light from the LAr target into the visible spectrum. This light is detected by 255 “inner” photomultiplier tubes (PMTs) which are optically coupled to the AV by acrylic light guides. The PMTs are distributed in “rings” around the AV, the PMTs in each ring having the same vertical position. The AV and PMTs are enclosed in a stainless steel shell which is continuously flushed with radon-scrubbed nitrogen gas. Installed on the outer surface of the shell are 48 “outer” PMTs looking outward which, combined with the water held within a cylindrical tank surrounding the detector, act as a muon veto system. A schematic of the detector is shown in Figure 1.

Temperature sensors are placed around the AV at 85 locations along filler blocks which are mounted in the spaces between the PMTs. The sensors are spread around the AV and placed at distances of 0.9 m, 1.1 m, or 1.3 m from the centre of the AV. These sensors, along with the temperature and pressure within the  $\text{LN}_2$  cooling system, are monitored and logged using a slow control system.

Within the data acquisition system (DAQ) each PMT is connected to a channel on a custom-built signal conditioning board (SCB) which achieves the high voltage decoupling and shapes the signal. The SCB outputs are transmitted to high-gain (CAEN V1720) and low-gain (CAEN V1740) waveform

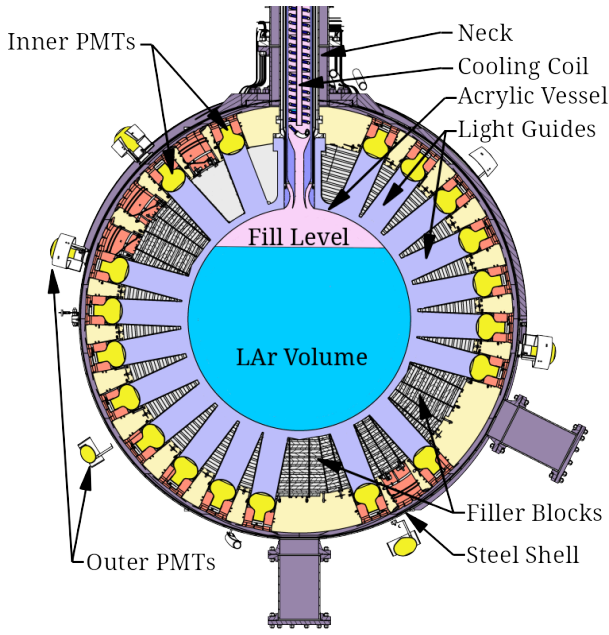


**Fig. 1** A cross-section of the DEAP-3600 detector components located inside the water Cherenkov muon veto detector (not shown).

digitizers. These digitizers convert a continuous analogue signal to a discrete digital signal using analogue-to-digital converters (ADCs). The summed input from each SCB is also passed to a digitizer and trigger module (DTM) which resolves the trigger criteria based on two rolling charge integrals: a narrow integral  $Q_n$  over a 177 ns window and a wide integral  $Q_w$  over a 3.1  $\mu$ s window. The promptness of the signal is computed by the  $Q_n/Q_w$  fraction. Five trigger regions are defined based on these three variables and a prescaling factor of 100 is applied to events in the energy range of  $Q_n \approx 50 - 565$  keV<sub>ee</sub> in the low  $Q_n/Q_w$  region. This prescaling predominantly affects  $^{39}\text{Ar}$  decays and reduces the available statistics by storing only the observed PMT waveforms for 1 out of every 100 events. The timestamp of every event, included those which are prescaled, is recorded in the data.

The DTM makes triggering decisions based on the value of  $Q_n$  and sends a trigger signal to the digitizers if this value passes the set trigger threshold. Each digitizer channel records PMT waveforms for 16  $\mu$ s upon receiving a trigger signal, including a pre-trigger window of 2.4  $\mu$ s. The data acquisition system is operated by MIDAS [18] and the data are analyzed with RAT [19], a software framework built on Geant4 [20] and ROOT [21]. The observed charge in each PMT is integrated and divided by the single photoelectron (PE) charge for each PMT measured through independent calibration [22]. The resulting PE number provides the energy estimator for the data. The pulse-shape discrimination (PSD) variable  $F_{\text{prompt}}$  distinguishes nuclear recoil events at high  $F_{\text{prompt}}$  from  $^{39}\text{Ar}$  decays and other electron recoil

backgrounds (ERB) at low  $F_{\text{prompt}}$ ; for this measurement it is defined as the fraction of PE detected in a time window of [-28, 150] ns around the event time:

$$F_{\text{prompt}} = \frac{\sum_{t=-28\text{ ns}}^{150\text{ ns}} PE(t)}{\sum_{t=-28\text{ ns}}^{10\text{ }\mu\text{s}} PE(t)} \quad (2)$$

The ERB is composed of events generated by both  $\gamma$ -rays emitted by trace radioactivity in detector components and  $\beta$ -decays which scatter on electrons in the LAr.

### 3 Liquid Argon Mass Estimate

The LAr mass is determined by evaluating both its density and its volume within the AV. This method previously resulted in a LAr mass of  $(3279 \pm 96)$  kg [15]. That result has been refined for this work.

Two inputs are required to evaluate the volume of LAr in the detector: the AV radius and the LAr height within the AV. The internal radius of the AV was measured during its construction. After correcting for the thermal contraction that occurred during cool-down using a temperature-dependent coefficient measured in Ref. [23] the AV radius is determined to be  $845.6 \pm 0.9$  mm. The LAr height is measured by taking advantage of the total internal reflection of the UV light at the GAR/LAr interface. The TPB re-emits light isotropically and so the photon detection rates for each PMT depend on the area of visible TPB immersed in the LAr. The rates for every PMT ring are averaged and the distribution is fit with an analytic model of the corresponding immersed area. This method is validated by comparing data to Monte Carlo simulations with different LAr height values. The best fit is found at a LAr height of  $(550 \pm 10)$  mm above the equator and is stable across the dataset. The systematic uncertainty on the LAr height is the dominant source of uncertainty for the LAr mass estimate. A cross-check using the position reconstruction of detected events to evaluate the LAr height provides a consistent result. In this cross-check, a template fit in the reconstructed vertical position of  $^{39}\text{Ar}$  decay events is performed by comparing simulations with different LAr height values to the data histogram.

The LAr density is a function of its temperature. This temperature is constrained by the liquid-vapor transition of the argon in the AV and by the liquid-vapor transition of the nitrogen in the cooling coil. As the pressure in both systems is constantly recorded, the average LAr temperature is known within a few degrees K, and thus the effective density can be established to 0.5% precision.

The possibility of argon bubbles is also investigated, the presence of which would reduce the total mass of LAr. Using the behavior of nitrogen as a reference [24] a limiting case is considered where all of the exterior heat entering the LAr

creates bubbles. This worst-case scenario indicates that at most 6.3 kg of LAr is displaced by bubbles.

A toy Monte Carlo sampling the probability distribution functions (PDFs) of the AV radius, LAr height, LAr density and bubble displacement is used to determine the central value of the LAr mass and its uncertainty. Flat PDFs are used for the constraints on the LAr density and the bubble displacement, while the AV radius and LAr height PDFs are considered Gaussian. According to this method, during the data-taking period of this measurement the DEAP-3600 AV contained  $m_{\text{LAr}} = (3269 \pm 24)$  kg of LAr.

## 4 Data Selection and Livetime Calculation

### 4.1 Run Selection

The dataset is divided into discrete runs during which signals from the LAr are recorded. A single run is typically about 22 hours long, though this can vary between just a few minutes and up to about 2 days. The runs examined here are from the same 2016-2017 dataset used for the dark matter search published by the DEAP collaboration [15] with the additional restriction that runs are at least 18 hours long. This requirement is imposed to ensure sufficient statistics to fit the gamma-dominated region of the ERB spectrum in each run.

The selection of runs is based on stability criteria concerning the cooling system of the AV, charge distributions in the PMTs, and efficiency of the trigger. A data cleaning cut is applied to each run to reject events occurring within  $\delta t_{\text{cut}} = 32 \mu\text{s}$  of the previous event, which removes  $\delta t_i \leq 32 \mu\text{s}$  of livetime per event  $i$ ; the total number of events removed by this cut is  $N_{\text{DCut}}$ . Low-level cuts are then applied to reject events recorded from pulse injections by periodic monitoring triggers and events with inconsistent data acquisition readouts such as busy signals, for a total of  $N_{\text{LLcut}}$  events. The events removed by these cuts, along with all remaining physics triggers  $N_{\text{phys}}$ , are taken into account in the run-dependent livetime calculation:

$$T_{\text{live}} = T_{\text{run}} - \sum_{i=1}^{N_{\text{DCut}}} \delta t_i - N_{\text{LLcut}} \cdot \delta t_{\text{cut}} - N_{\text{phys}} \cdot (\delta t_{\text{cut}} - \delta t_{\text{int}}) \quad (3)$$

where  $T_{\text{live}}$  is the livetime for a run,  $T_{\text{run}}$  is the total time of that run, and  $\delta t_{\text{int}} = 10 \mu\text{s}$  corresponds to the charge integration window during which the detector can record a pile-up event, while the time between  $\delta t_{\text{int}}$  and  $\delta t_{\text{cut}}$  is dead time. The value of  $N_{\text{phys}}$  includes the prescaled triggers as the timestamp of each of these events is stored. An offline reduction is applied where only 1 out of every 100 events from outside the prescaled trigger region is kept in order to remove boundary effects and obtain a smooth spectrum. A

typical 22-hour run provides roughly  $2.5 \times 10^6$  events due to  $^{39}\text{Ar}$  after all prescaling is applied.

### 4.2 Event Selection

In addition to the data cleaning and low-level cuts described in the previous section, event selection cuts are applied. Pile-up needs to be taken into account given the high rate of  $^{39}\text{Ar}$  decays and the length of the event window: approximately 5% of recorded events are expected to contain 2 or more decays. Additionally, a triggered event can follow an energy deposit which happened during dead time within the DAQ. The late scintillation light from this previous, unrecorded energy deposit can reach into the beginning of the triggered event. Since the full energy of the previous energy deposit is not visible in the digitized trace this type of pile-up is hard to model. While this analysis endeavours to keep pile-up events and account for them in the specific activity calculation, events with this pre-trigger pileup are not suitable analysis candidates.

To select events for which there is no pre-trigger pile-up, the time at which the event occurred within the trigger window must be between 2250 ns and 2700 ns, and it is required that fewer than 4 pulses are recorded by the PMTs in the first 1600 ns of the event. Electron recoil events, which are dominated by  $^{39}\text{Ar}$  decays at lower energies and gamma backgrounds at higher energies as shown in Figure 2, are selected with the requirement  $0.1 \leq F_{\text{prompt}} \leq 0.5$ . This analysis also makes use of a peak-finding algorithm based on the PMT waveforms' slope, to count the number of "sub-events" identified within the trigger window. The number of sub-events is used to select pile-up candidates in order to perform a data-driven estimate of the double  $^{39}\text{Ar}$  pile-up cut efficiency as described in Section 5.2.

## 5 Specific Activity Measurement

The  $^{39}\text{Ar}$  specific activity is measured individually for each run in the dataset. Each measurement is based on a fit to the low  $F_{\text{prompt}}$  energy spectrum and consists of an  $^{39}\text{Ar}$   $\beta$ -decay spectrum (single  $^{39}\text{Ar}$ ), a spectrum with two  $^{39}\text{Ar}$  decays occurring within the same trigger window (double  $^{39}\text{Ar}$  pile-up), and a spectrum containing all non- $^{39}\text{Ar}$  ERB events scaled to the activities measured in Ref. [16]. The ERB and double  $^{39}\text{Ar}$  pile-up input spectra are generated by simulating events within the DEAP-3600 detector using the RAT software. The single  $^{39}\text{Ar}$  component is built directly from the theoretical model provided by Kostensalo et al. [25]. Each of the three model components is normalized using a parameter in the fits. Energy scale and detector resolution effects in the form of a Gaussian term are applied to all three

model components, parameterized as

$$PE = p_0 + p_1 \cdot E + p_2 \cdot E^2$$

$$\sigma(PE) = \sqrt{p_3 \cdot PE + p_4 \cdot PE^2} \quad (4)$$

The constant energy scale parameter  $p_0$  is fixed in the fits to a value obtained by measuring PMT signals preceding the detected event. The number of  $^{39}\text{Ar}$  decays is split into two main components

$$N = N_{\text{single}} + N_{\text{pile-up}} \quad (5)$$

with the number of single  $^{39}\text{Ar}$  decays  $N_{\text{single}}$  and the number of  $^{39}\text{Ar}$  decays which are part of a pile-up event  $N_{\text{pile-up}}$ . The latter number includes double  $^{39}\text{Ar}$  decays, triple  $^{39}\text{Ar}$  decays (three  $^{39}\text{Ar}$  decays in one trigger window), pile-up of  $^{39}\text{Ar}$  decays with ERB decays, and pile-up of  $^{39}\text{Ar}$  decays with high  $F_{\text{prompt}}$  events ( $F_{\text{prompt}} > 0.5$ ).

### 5.1 Fitting the Energy Spectrum

This analysis uses Minuit in ROOT [26] to fit the three input spectra to data. The fit minimizes

$$\chi^2 = \sum_i^{n_b} \left( \frac{M_i - D_i}{\sqrt{M_i}} \right)^2 + \mathcal{P} \quad (6)$$

with the number of bins  $n_b$  in the data histogram, the data content  $D_i$  in bin  $i$  and the model contribution  $M_i$ .  $\mathcal{P}$  is a penalty term applied to a shape nuisance parameter  $a_0$ , which corrects the theoretical  $^{39}\text{Ar}$  input spectrum linearly in energy to fit the data and is constructed to account for the differences  $\Delta a_0 = 0.01$  observed between the Kostensalo et al. [25] and the Behrens & Janecke [27]  $^{39}\text{Ar}$   $\beta$ -shapes:

$$\mathcal{P} = \frac{a_0}{\Delta a_0} \quad (7)$$

The closer  $a_0$  is to zero, the more the spectrum fits the shape by Kostensalo et al. The fit model is adapted from the model used for the energy response fits in Ref. [15]. This analysis is performed with  $n_b$  corresponding to a bin width of  $b = 20$  PE to provide sufficient statistics in each histogram bin.

The fit range for this measurement, 200–11,000 PE is chosen to avoid trigger efficiency effects at low PE and to provide a handle for the fit to scale  $n_{\text{double}}$  and  $n_{\text{ERB}}$  beyond the  $^{39}\text{Ar}$  endpoint at high PE. This range includes the  $^{40}\text{K}$   $\gamma$ -emission peak at 1460 keV [16] and allows the ERB spectrum normalization to be determined in the fit. The  $^{39}\text{Ar}$   $\beta$ -shape nuisance parameter is an output of the fit. Details of the fit inputs and outputs are provided in Table 1, along with the other parameter values taken as input to the specific activity measurement. Figure 2 shows an example fit using this model for one data run.

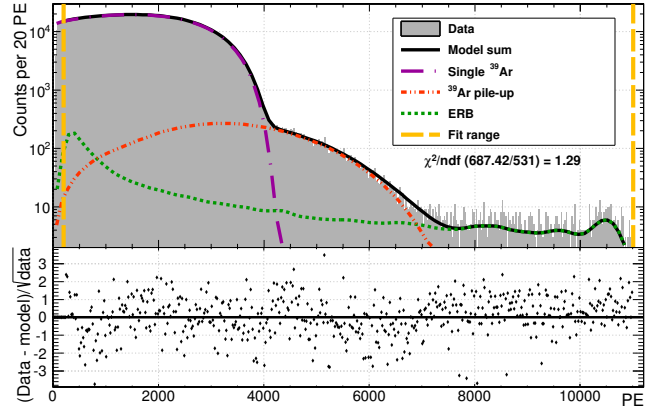


**Fig. 2** The top panel shows an example fit on one run including the  $^{39}\text{Ar}$ , ERB, and  $^{39}\text{Ar}$  pile-up components which form the fit function. The fit range from 200–11,000 PE is shown by the vertical dashed lines. The bottom panel shows the residual between the fit function and data normalized to the square root of the contents in the observed PE distribution. The run shown here is approximately 28.5 hours long.

### 5.2 Calculating the Specific Activity

The number of  $^{39}\text{Ar}$  single decays  $N_{\text{single}}$  is obtained from the integral of the single  $^{39}\text{Ar}$  spectrum fit result  $n$ :

$$N_{\text{single}} = \frac{n \cdot a_{\text{presc}}}{\varepsilon \cdot b} \quad (8)$$

with the bin width  $b$  of the fitted data histogram, a trigger prescaling correction factor  $a_{\text{presc}} = 100$  and the cut efficiency  $\varepsilon$ . The main, data-driven method used to estimate this cut efficiency involves defining a loose event selection for the denominator spectrum with an  $F_{\text{prompt}} < 0.7$  requirement; the numerator spectrum contains those events that pass the selection cuts described in Section 4.2. First, the efficiency  $\varepsilon_{\text{lowerPE}}$  is calculated over the range 300–3000 PE which is dominated by single  $^{39}\text{Ar}$  events, by taking the ratio of the two spectra bin-by-bin. Then, to extract the efficiency  $\varepsilon$  for single  $^{39}\text{Ar}$  events, a correction is applied to  $\varepsilon_{\text{lowerPE}}$  to account for the presence of double  $^{39}\text{Ar}$  pile-up in the sample. The cut efficiency  $\varepsilon_{\text{double}}$  is calculated bin-by-bin in the PE histogram of each run over the range 200–8000 PE with an additional event selection requirement for the numerator and denominator spectra to select events which contain exactly two sub-events. The efficiency for single  $^{39}\text{Ar}$  events is then calculated by solving for  $\varepsilon$  in the following equation:

$$\varepsilon_{\text{lowerPE}} = \varepsilon \cdot x + \varepsilon_{\text{double}} \cdot (1 - x), \quad (9)$$

where  $x \sim 0.992$  is the fraction of single  $^{39}\text{Ar}$  events measured by the fits in the lower-PE range 300–3000 PE. The resulting data-driven value of  $\varepsilon$  is calculated run-by-run. The average  $\varepsilon$  is 0.983, with small variations taken into account for each run across the dataset.

As a cross-check to this data-driven method, the cut efficiency values are evaluated using the Monte Carlo simulated

**Table 1** Parameters, their values and constraints, and the resulting contributions to the uncertainty for the specific activity measurement. Negligibly small systematic uncertainties are indicated with ‘–’. The dominant uncertainty on  $S_{\text{Ar39}}$  arises from the uncertainties on event selection cut efficiency values as determined with the data-driven method (d-d) and the Monte Carlo method (MC).

Parameter	Symbol	Value	Constraints	Absolute uncertainty on $S_{\text{Ar39}}$ [Bq/kg <sub>atmAr</sub> ]
Fit range		200–11000 PE	Fixed	0.001
Histogram bin width	$b$	20 PE	Fixed	0.001
Constant energy scale parameter	$p_0$	$(1.3 \pm 0.4)$ PE	Fixed	–
Linear energy scale term	$p_1$	$[7.1 \text{ to } 7.3]$ PE/keV	Free-floating, run-dependent	0.009
Quadratic energy scale term	$p_2$	–	Not considered in this method	–
Linear resolution parameter	$p_3$	$[1.67 \text{ to } 1.73]$ PE	Free-floating, run-dependent	0.009
Quadratic resolution parameter	$p_4$	$[2.1 \text{ to } 3.8] \times 10^{-4}$	Free-floating, run-dependent	0.001
$^{39}\text{Ar}$ $\beta$ -shape nuisance parameter	$a_0$		Free-floating, constrained by a penalty term	0.001
$^{39}\text{Ar}$ normalization	$n$		Free floating, run-dependent	–
Double $^{39}\text{Ar}$ pile-up normalization	$n_{\text{double}}$		Free floating, run-dependent	–
ERB normalization	$n_{\text{ERB}}$		Free-floating, run-dependent	–
$^{85}\text{Kr}$ normalization	$n_{\text{Kr85}}$		Upper limit, see Section 5.2	0.010
Liquid argon mass	$m_{\text{LAr}}$	$(3269 \pm 24)$ kg	Measured, see Section 3	0.007
Live-time	$T_{\text{live}}$	167 d [sum of all runs]	Measured, see Section 4	–
Cut efficiency on single $^{39}\text{Ar}$	$\epsilon$	0.983 [d-d], 0.999 [MC]	Measured, see Section 5.2	0.016
Cut efficiency on double $^{39}\text{Ar}$ pile-up	$\epsilon_{\text{double}}$	Run- & energy-dependent		

samples of  $^{39}\text{Ar}$  decays and double  $^{39}\text{Ar}$  pile-up described earlier. While the simulations do not describe data perfectly, with this method the purity of the samples is guaranteed. With the Monte Carlo method  $\epsilon_{\text{MC}} = 0.999$ . We evaluate the specific activity  $S_{\text{Ar39}}$  using both  $\epsilon$  and  $\epsilon_{\text{MC}}$  as inputs to Eq. 8 and take the difference as a systematic uncertainty. This difference is the dominant source of systematic uncertainty for this measurement.

The number of  $^{39}\text{Ar}$  decays that are part of pile-up events is split into the different components:

$$N_{\text{pile-up}} = N_{\text{double}} + N_{\text{triple}} + N_{\text{ERB,Ar39}} + N_{\text{hFp,Ar39}} \quad (10)$$

Here,  $N_{\text{double}}$  is the number of  $^{39}\text{Ar}$  decays that are part of a double  $^{39}\text{Ar}$  pile-up event,  $N_{\text{triple}}$  is the number of  $^{39}\text{Ar}$  decays that are part of a triple pile-up event,  $N_{\text{ERB,Ar39}}$  is the number of  $^{39}\text{Ar}$  decays which pile-up with a ERB recoil, and  $N_{\text{hFp,Ar39}}$  is the number of  $^{39}\text{Ar}$  decays which pile-up with a high  $F_{\text{prompt}}$  process such as Cherenkov light or a nuclear recoil.  $N_{\text{double}}$  is obtained from the integral of the double  $^{39}\text{Ar}$  spectrum fit result  $n_{\text{double}}$ :

$$N_{\text{double}} = \frac{n_{\text{double}} \cdot a_{\text{presc}}}{\epsilon_{\text{double}} \cdot b} \cdot 2 \quad (11)$$

where  $\epsilon_{\text{double}}$  is the cut efficiency on double  $^{39}\text{Ar}$  pile-up events described above, and the factor 2 corrects for 2  $^{39}\text{Ar}$  decays in 1 double pile-up event. The energy-dependence of  $\epsilon_{\text{double}}$  over the wider range of the pile-up spectrum is taken into account by applying this correction bin-by-bin.

$N_{\text{double}}$  is utilized to calculate the total  $^{39}\text{Ar}$  rate  $R_{\text{Ar39}}$  from a first-order pile-up calculation:

$$R_{\text{Ar39}} = \sqrt{\frac{N_{\text{double}}}{2 \cdot T_{\text{live}} \cdot \delta t_{\text{int}}}} \quad (12)$$

$R_{\text{Ar39}}$  is used to determine the remaining pile-up components which are estimated with first-order pile-up approximations:

$$\begin{aligned} N_{\text{triple}} &= 3 \cdot R_{\text{Ar39}}^3 \cdot \delta t_{\text{int}}^2 \cdot T_{\text{live}} \\ N_{\text{ERB,Ar39}} &= R_{\text{Ar39}} \cdot R_{\text{ERB}} \cdot \delta t_{\text{int}} \cdot T_{\text{live}} \\ N_{\text{hFp,Ar39}} &= R_{\text{Ar39}} \cdot R_{\text{hFp}} \cdot \delta t_{\text{int}} \cdot T_{\text{live}} \end{aligned} \quad (13)$$

The ERB rate  $R_{\text{ERB}} = (10.5 \pm 0.6)$  Hz and the high  $F_{\text{prompt}}$  rate  $R_{\text{hFp}} = (270 \pm 3)$  Hz are reestablished from the fit output  $n_{\text{ERB}}$  and from the rate of events observed in the high  $F_{\text{prompt}}$  window in the dataset.

Beyond the ERB measured in Ref. [16], the dataset considered in this analysis may contain a small number of  $^{85}\text{Kr}$   $\beta$ -decay events. Uncertainty in the amplitude of a peak at 600.66 keV from the  $^{226}\text{Ra}$  chain makes obtaining the  $^{85}\text{Kr}$  from fitting the energy spectrum challenging. This is studied a posteriori by repeating the fit including the  $^{85}\text{Kr}$   $\beta$ -shape from Ref. [28] with a normalization parameter  $n_{\text{Kr85}}$ , while also varying the energy response parameters and the  $^{39}\text{Ar}$  endpoint within their uncertainties. These fit results suggest that at most 0.01 Bq/kg<sub>atmAr</sub> of  $^{85}\text{Kr}$  is present in our dataset. This limit is considered as an additional source of systematic uncertainty.

### 5.3 Results

The specific activity of  $^{39}\text{Ar}$  is evaluated for each run by combining Eqs. 8, 11 and 13 with Eq. 1. The run-by-run results are presented in Figure 3 which includes an exponential fit to the measured specific activity over time. This fit is used to determine the specific activity value at the start of the dataset.

Uncertainties due to the liquid argon mass estimate and related to the determination of cut efficiencies are discussed in Sections 3 and 5.2 respectively. Additional systematic uncertainties on the specific activity measurement are evaluated as follows. For each run, the fit is repeated with the linear energy scale parameter  $p_1$  fixed to its central value for that run plus or minus 0.15 PE/keV. The uncertainties on the other energy scale and resolution parameters  $p_0$ ,  $p_3$  and  $p_4$  are likewise propagated to the measurement by repeating the fits with fixed parameters set according to their uncertainties determined in the energy response measurement described in Ref. [15]. Uncertainties due to the choice of histogram bin width (varied to 10 PE and 40 PE) and the choice of fit range (lower bound increased to 500 PE) are evaluated in a similar fashion. Theoretical  $\beta$ -shape uncertainties are accounted for by repeating the fit with  $a_0$  fixed to 0, and then fixed to the median value found over the entire dataset. The impact of each source of systematic uncertainty on the result is detailed in Table 1.

The statistical uncertainty of  $\pm 0.001 \text{ Bq/kg}_{\text{atmAr}}$  shown in Figure 3 is calculated from counting uncertainties on ERB and high  $F_{\text{prompt}}$  backgrounds, and the fit uncertainties on the single  $^{39}\text{Ar}$  and the double  $^{39}\text{Ar}$  pile-up scaling parameters.

A correction is applied to the measured specific activity determined from the exponential fit, to account for the age of the argon. The correction factor is

$$\eta_t = 2^{(t_{\text{age}}/T_{1/2})}, \quad (14)$$

where  $t_{\text{age}} = (1.0 \pm 0.5) \text{ y}$  is the average time between atmospheric extraction of the argon and the start of the data-taking period. Multiplying by  $\eta_t$  corrects for the approximately 0.26 % drop in activity before data were taken. Cosmogenic activation of  $^{39}\text{Ar}$  in the time after the argon was extracted from the atmosphere is negligible.

The specific activity of  $^{39}\text{Ar}$  in atmospheric argon is measured to be

$$S_{\text{Ar}39} = [0.964 \pm 0.001(\text{stat}) \pm 0.024(\text{sys})] \text{ Bq/kg}_{\text{atmAr}} \quad (15)$$

### 6 Cross-Check Analysis

An earlier analysis, the details of which are described in Ref. [17], used the Bayesian Analysis Toolkit (BAT) [29] software which uses Markov Chain Monte Carlo to estimate the model parameters from posterior probability distributions. That result has been updated and is presented here

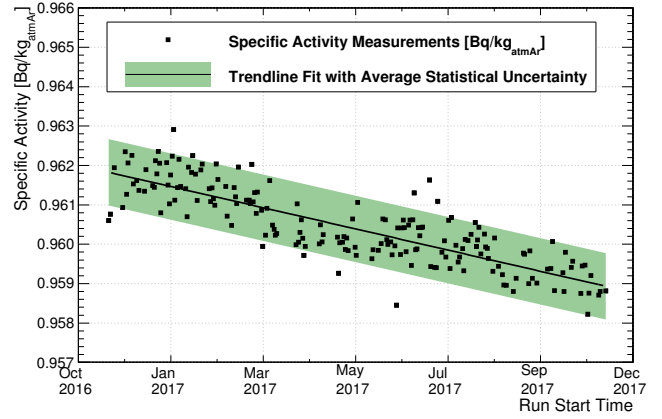


**Fig. 3** The measured specific activity of  $^{39}\text{Ar}$  versus run time for the entire dataset. The exponential trendline fit is shown, with the average statistical uncertainty depicted as an error band. The systematic uncertainty band is wider than the y-axis shown here.

as a cross-check. This cross-check differs from the analysis presented in previous sections by making an alternate set of event selection cuts. A cut on the event time within the trigger window was not applied, and the peak-finding algorithm to count “sub-events” was used to remove the majority of pileup events. The data cleaning cut to remove events close in time to a previous event was not applied. Otherwise the same criteria described in Section 4 were applied and a fit was performed on each run in the dataset.

The detector response model in the fit included a constant energy scale parameter  $p_0$ , a linear energy scale parameter  $p_1$ , a quadratic energy scale parameter  $p_2$ , and a linear resolution parameter  $p_3$ . The quadratic resolution parameter  $p_4$  was not considered in these fits. The  $p_1$ ,  $p_2$ , and  $p_3$  model parameters were given flat priors in the fits and allowed to float. The  $p_0$  parameter was fixed in the fits.

The input  $^{39}\text{Ar}$  spectrum used was from Behrens & Jänekke [27]. Each fit returned the normalization of this spectrum and was given a flat prior. In addition to the  $^{39}\text{Ar}$  spectrum, the inputs to the fit were an ERB spectrum and an MC-generated spectrum of double  $^{39}\text{Ar}$  pileup events which survive the cuts. Each fit returned the normalization parameters for these spectra; at the input stage these were given Gaussian priors with a mean value of 1, which corresponded to a normalization based on an assumed event rate and the known runtime. All three normalization parameters were allowed to float in the fits, and the posterior values were used to calculate the  $^{39}\text{Ar}$  specific activity.

The result in Ref. [17] has been updated here to include the updated LAr mass, the new data-driven cut efficiency estimates, the revised livetime calculation, and the correction for the age of the argon. This method yields the following value for the specific activity of  $^{39}\text{Ar}$  at the time of atmospheric extraction:  $[0.97 \pm 0.001(\text{stat}) \pm 0.03(\text{sys})] \text{ Bq/kg}_{\text{atmAr}}$ .

**Table 2** Summary of specific activity measurements of  $^{39}\text{Ar}$  by different collaborations.

Measurement	Specific activity [ $\text{Bq/kg}_{\text{atmAr}}$ ]
WARP [13]	$1.01 \pm 0.08$
ArDM [14]	$0.95 \pm 0.05$
DEAP-3600 (this work)	$0.964 \pm 0.024$

## 7 Conclusion

A measurement of the specific activity of  $^{39}\text{Ar}$  in atmospheric argon using the LAr target of the DEAP-3600 detector has been presented. This result is the most precise measurement of the specific activity of  $^{39}\text{Ar}$  in atmospheric argon to date and agrees with existing measurements which are summarized in Table 2. The high precision of this measurement is owing to a combination of factors including the low-background nature of DEAP-3600, the large number of observed  $^{39}\text{Ar}$  decays, and the precise measurement of the LAr target mass. The statistical uncertainties here are much smaller than the systematic uncertainties due to the high statistics of the data. The dominant systematic uncertainties arise from the event selection cut efficiencies, the energy scale and energy resolution parameters, and the possible presence of  $^{85}\text{Kr}$  within the LAr.

**Acknowledgements** We thank the Natural Sciences and Engineering Research Council of Canada (NSERC), the Canada Foundation for Innovation (CFI), the Ontario Ministry of Research and Innovation (MRI), and Alberta Advanced Education and Technology (ASRIP), the University of Alberta, Carleton University, Queen's University, the Canada First Research Excellence Fund through the Arthur B. McDonald Canadian Astroparticle Physics Research Institute, Consejo Nacional de Ciencia y Tecnología Project No. CONACYT CB-2017-2018/A1-S-8960, DGAPA UNAM Grants No. PAPIIT IN108020 and IN105923, and Fundación Marcos Moshinsky, the European Research Council Project (ERC StG 279980), the UK Science and Technology Facilities Council (STFC) (ST/K002570/1 and ST/R002908/1), the Leverhulme Trust (ECF-20130496), the Russian Science Foundation (Grant No. 21-72-10065), the Spanish Ministry of Science and Innovation (PID2019-109374GB-I00) and the Community of Madrid (2018-T2/TIC-10494), the International Research Agenda Programme AstroCeNT (MAB/2018/7) funded by the Foundation for Polish Science (FNP) from the European Regional Development Fund, and the European Union's Horizon 2020 research and innovation program under grant agreement No 952480 (DarkWave). Studentship support from the Rutherford Appleton Laboratory Particle Physics Division, STFC and SEPNet PhD is acknowledged. We thank SNOLAB and its staff for support through underground space, logistical, and technical services. SNOLAB operations are supported by the CFI and Province of Ontario MRI, with underground access provided by Vale at the Creighton mine site. We thank Vale for their continuing support, including the work of shipping the acrylic vessel underground. We gratefully acknowledge the support of the Digital Research Alliance of Canada, Calcul Québec, the Centre for Advanced Computing at Queen's University, and the Computational Centre for Particle and Astrophysics (C2PAP) at the Leibniz Supercomputer Centre (LRZ) for providing the computing resources required to undertake this work.

## References

1. G. Fiorillo, Nuc. Phys. B Proc. Sup. **150**, 372 (2006)
2. G. Aad et al. (ATLAS Collaboration), Eur. Phys. J. C **70**, 723 (2010)
3. P.D. Meyers et al. (DarkSide Collaboration), Physics Procedia **61**, 124 (2015)
4. M. Agostini et al., Eur. Phys. J. C **75**, 506 (2015)
5. B. Abi et al. (DUNE Collaboration), Journal of Instrumentation **15**(12), P12004 (2020)
6. P. Abratenko et al. (MicroBooNE Collaboration), Phys. Rev. Lett. **130**, 011801 (2023)
7. P.-A. Amaudruz et al. (DEAP Collaboration), Astropart. Phys. **108**, 1 (2019)
8. A.N. Cox (ed.), *Allen's Astrophysical Quantities*, 4th edn. (Springer, New York, 2001)
9. H. Loosli, Earth and Planetary Science Letters **63**(1), 51 (1983)
10. R.W. Stoenner, O.A. Schaeffer, S. Katcoff, Science **148**(3675), 1325 (1965)
11. M. Wang, et al., Chinese Physics C **36**(12), 003 (2012)
12. J.Q. Gu, A.L. Tong, G.M. Yang, S.M. Hu, W. Jiang, Z.T. Lu, R. Purtschert, F. Ritterbusch, Chemical Geology **583**, 120480 (2021)
13. P. Benetti et al. (WARP Collaboration), Nucl. Instrum. Methods Phys. Res. A **574**(1), 83 (2007)
14. J. Calvo et al. (ArDM Collaboration), Journal of Cosmology and Astroparticle Physics **2018**(12), 011 (2018)
15. R. Ajaj et al. (DEAP Collaboration), Phys. Rev. D **100**, 022004 (2019)
16. R. Ajaj et al. (DEAP Collaboration), Phys. Rev. D **100**, 072009 (2019)
17. M. Dunford, A Search for the Neutrinoless Double Electron Capture of  $^{36}\text{Ar}$  and a Measurement of the Specific Activity of  $^{39}\text{Ar}$  in Atmospheric Argon with the DEAP-3600 Detector. Ph.D. thesis, Carleton University, Department of Physics (2018)
18. T. Lindner, Journal of Physics: Conference Series **664**(8), 082026 (2015)
19. T. Bolton, et al. RAT (is an Analysis Tool) User's Guide (2018). URL <https://rat.readthedocs.io/en/latest/>
20. S. Agostinelli et al. (GEANT4 Collaboration), Nucl. Instrum. Methods Phys. Res. A **506**(3), 250 (2003)
21. R. Brun, F. Rademakers, Nucl. Instrum. Methods Phys. Res. A **389**(1), 81 (1997), New Computing Techniques in Physics Research V
22. P.-A. Amaudruz et al. (DEAP Collaboration), Nucl. Instrum. Methods Phys. Res. A **922**, 373 (2019)
23. G. Hartwig, *Polymer Properties at Room and Cryogenic Temperatures* (Plenum Press, New York, 1994)
24. N. Fdida et al., ILASS – Europe 2010, 23rd Annual Conference on Liquid Atomization and Spray Systems

- 
- (2010)
25. J. Kostensalo, J. Suhonen, K. Zuber, *Journal of Physics G Nuclear Physics* **45**(2), 025202 (2018)
  26. F. James, M. Winkler. MINUIT User's Guide (2004).  
URL <https://inspirehep.net/literature/1258345>
  27. H. Behrens, J. Jänecke. 2.3 Special formulae for allowed, first forbidden, L-th non unique forbidden, and (L-1)-th-unique forbidden beta-decays: Datasheet from Landolt-Börnstein - Group I Elementary Particles, Nuclei and Atoms · Volume 4: "Numerical Tables for Beta-Decay and Electron Capture" in SpringerMaterials (1969)
  28. S.J. Haselschwardt, J. Kostensalo, X. Mougeot, J. Suhonen, *Phys. Rev. C* **102**, 065501 (2020)
  29. A. Caldwell, D. Kollár, K. Kröninger, *Computer Physics Communications* **180**(11), 2197 (2009)